



symmetry

IMPACT
FACTOR
2.7

CITESCORE
4.9

Article

Combined Analysis of Neutrino and Antineutrino Charged Current Inclusive Interactions

Juan M. Franco-Patino, Alejandro N. Gacino-Olmedo, Jesus Gonzalez-Rosa, Stephen J. Dolan, Guillermo D. Megias, Laura Munteanu, Maria B. Barbaro and Juan A. Caballero

Special Issue

Symmetry and Neutrino Physics: Theory and Experiments

Edited by








Prof. Dr. Antonia Di Crescenzo and Prof. Dr. Giuliana Galati



<https://doi.org/10.3390/sym16050592>

Article

Combined Analysis of Neutrino and Antineutrino Charged Current Inclusive Interactions

Juan M. Franco-Patino ^{1,†}, Alejandro N. Gacino-Olmedo ^{1,2,†}, Jesus Gonzalez-Rosa ^{1,†}, Stephen J. Dolan ², Guillermo D. Megias ^{1,*}, Laura Munteanu ², Maria B. Barbaro ^{3,4} and Juan A. Caballero ¹

¹ Departamento de Física Atómica, Molecular y Nuclear, Universidad de Sevilla, 41080 Sevilla, Spain; jfpatino@us.es (J.M.F.-P.); alejandro.nicolas.gacino.olmedo@cern.ch (A.N.G.-O.); jgroso@us.es (J.G.-R.); jac@us.es (J.A.C.)

² European Organization for Nuclear Research (CERN), CH-1211 Geneva, Switzerland; stephen.joseph.dolan@cern.ch (S.J.D.); laura.munteanu@cern.ch (L.M.)

³ Dipartimento di Fisica, Università di Torino, Via P. Giuria 1, 10125 Torino, Italy; barbaro@to.infn.it

⁴ INFN, Sezione di Torino, Via P. Giuria 1, 10125 Torino, Italy

* Correspondence: megias@us.es

† These authors contributed equally to this work and share first authorship.

Abstract: This paper presents a combined analysis of muon neutrino and antineutrino charged-current cross sections at kinematics of relevance for the T2K, MINERvA and MicroBooNE experiments. We analyze the sum, difference and asymmetry of neutrino versus antineutrino cross sections in order to get a better understanding of the nuclear effects involved in these processes. Nuclear models based on the superscaling behavior and the relativistic mean field theory are applied, covering a wide range of kinematics, from hundreds of MeV to several GeV, and the relevant nuclear regimes, i.e., from quasilelastic reactions to deep inelastic scattering processes. The NEUT neutrino-interaction event generator, used in neutrino oscillation experiments, is also applied to the analysis of the quasielastic channel via local Fermi gas and spectral function approaches.

Keywords: weak interactions; neutrino oscillations; asymmetry; neutrino interactions; neutrino cross sections; long-baseline neutrino experiments; neutrino-nucleus scattering; neutrino antineutrino; relativistic mean field; superscaling



Citation: Franco-Patino, J.M.; Gacino-Olmedo, A.N.; Gonzalez-Rosa, J.; Dolan, S.J.; Megias, G.D.; Munteanu, L.; Barbaro, M.B.; Caballero, J.A. Combined Analysis of Neutrino and Antineutrino Charged Current Inclusive Interactions. *Symmetry* **2024**, *16*, 592. <https://doi.org/10.3390/sym16050592>

Academic Editors: Giuliana Galati and Antonia Di Crescenzo

Received: 19 March 2024

Revised: 11 April 2024

Accepted: 19 April 2024

Published: 10 May 2024



Copyright: © 2024 by the authors. Licensee MDPI, Basel, Switzerland. This article is an open access article distributed under the terms and conditions of the Creative Commons Attribution (CC BY) license (<https://creativecommons.org/licenses/by/4.0/>).

1. Introduction

The study of the properties of neutrinos (and antineutrinos) in connection with charge-parity violation (CPV) in weak interactions is a topic of great interest in modern particle physics [1,2]. Current neutrino oscillation experiments are entering a high-precision era to determine the CP violating phase δ_{CP} that defines the different behavior of particles and antiparticles in the weak sector under the three-flavor PMNS neutrino-mixing paradigm [2–4]. In oscillation experiments, some evidence for differences in oscillation characteristics for neutrinos and antineutrinos have been already observed [5], indicating a first evidence of this CP violation. An accurate determination of the δ_{CP} phase is expected in coming experiments such as HyperKamiokande or DUNE [6,7]. The success of this challenging task largely depends on a reduction of current experimental uncertainties, mostly related to flux and cross section modeling [8]. A particularly important challenge is the robust modeling of the differences in neutrino and antineutrino cross sections, such that observations in oscillation experiments can be correctly identified as genuine CP-violation or simply a cross-section mis-modelling. To this end, in this work we mostly focus on the analysis of the neutrino and antineutrino differences observed in the measurements of the T2K experiment [9], also showing neutrino-antineutrino differences at T2K and MINERvA kinematics when also considering the full inelastic regime.

Regarding nuclear dynamics, most past and current experiments—MiniBooNE, MicroBooNE, T2K, NOvA, MINERvA, ArgoNEUT—but also future ones—DUNE and HyperK [6,7,10–17]—operate in the 0.5–10 GeV region, where different reaction mechanisms play an important role in the nuclear response. In particular, the quasi-elastic (QE) channel, associated to one-nucleon knockout, is the dominant contribution in the range from hundreds of MeV to a few GeV of the incident neutrino energy. In this region it is also necessary to describe the emission of two nucleons, i.e., the so-called two-particle-two-hole (2p2h) channel, and the resonance (RES) regime, describing the excitation of nucleonic resonances followed by their decay and the subsequent emission of pions and other mesons. As the neutrino energies increases up to several GeV, not only the resonance regime but also other inelasticities, corresponding to non-resonant meson production and deep-inelastic scattering (DIS) processes, become more relevant. This energy region is of interest for some experiments such as MINERvA or ArgoNEUT, and will be essential for the next-generation DUNE experiment. Most current measurements are focused on measuring $CC0\pi$ (or “quasielastic-like”) events, which are defined as charged-current (CC) reactions with no pions (0π) detected in the final state and, thus, dominated by QE and 2p2h contributions. Nevertheless, the inelastic region is also analyzed in some of these experiments via CC-inclusive measurements, where no specific hadronic final state is selected, thus implying that all nuclear reaction mechanisms have to be considered. It is worth mentioning that the inelastic regime, which includes resonant and non-resonant meson production and deep-inelastic scattering, can also represent an important background in $CC0\pi$ data if, for example, the mesons emitted in the interaction are subsequently absorbed in the nuclear medium, thus mimicking a $CC0\pi$ event. In this regard, the excitation of nucleon resonances represents one of the most relevant inelastic channels, being related to larger transferred energies than the ones in the QE channel and involving higher final-state hadronic masses. The resonance regime has been extensively studied in previous works by different groups [18–25]. Emphasis has been placed not only on the description of the nucleonic resonances but also on the treatment of the nuclear effects introduced in the analysis of lepton-nucleus reactions.

Moreover, there is a lack of accurate models and specific measurements in the so-called Shallow Inelastic Scattering (SIS) region, that is, the transition region between the resonant and DIS regimes [21]. Information about the resonant nucleon form factors and the inelastic structure functions is mainly extracted from electron scattering data, which implies some restrictions when extended to the neutrino case, as the axial channel is missing in electron reactions. This extension thus requires relying on different approximations based on QCD calculations, quark models, and Parton Distribution Functions (PDFs) or semi-phenomenological models. Nonetheless, most of these approaches are affected by kinematical restrictions and large uncertainties, which makes it difficult to get a consistent and accurate description of the full inelastic regime. Note also that in the SIS region multiple processes emerge, including a continuum of higher order resonance states, a significant fraction of non-resonant processes, and low multiplicity DIS events, but at the same time processes with identical final states interfere making it difficult to quantify accurately the magnitude of the corresponding interference terms. Thus the SIS and DIS channels are currently a matter of continuous study [18,22–29], although more experimental studies and theoretical analysis at the kinematics of interest for oscillation experiments are still required.

In this context, several groups [30–33] have described the inelastic region, mainly pion production in nuclei, providing different descriptions of nuclear dynamics and the initial nuclear state, pion production in a bound nucleon, and the possible subsequent pion-nucleon interaction within the residual nucleus. Most of the initial studies were based on the simple Fermi gas approach of non-interacting nucleons, but recently more sophisticated descriptions have been developed, incorporating relativistic mean field nuclear potentials, Random Phase Approximation calculations or spectral functions. Regarding resonant production in the nucleon, several groups have also developed sophisticated approaches to analyze the nucleon structure in this regime, such as the MK model [34,35] or the Dynamical

Coupled-Channels (DCC) model [36–38], which have been tested against electron and neutrino scattering data.

2. General Formalism

In what follows, we summarize the framework used to describe the different nuclear regimes and reaction mechanisms addressed in this work.

2.1. QE Cross Sections

The superscaling approach (SuSA) is based on the scaling properties exhibited by inclusive electron scattering where the QE scattering cross section can be written, under certain conditions, as a term containing the single-nucleon cross section times a scaling function (f) that embodies the nuclear dynamics [39]. The analysis of inclusive electron scattering data [39] has shown that, for not too low transferred momentum (q larger than about 400 MeV/c), the scaling function does not depend on q (scaling of 1st kind) nor on the nuclear species (scaling of 2nd kind) and can therefore be expressed in terms of a single variable ψ , the so-called scaling variable. A more detailed description of superscaling can be found in refs. [39–44]. This approach has been also successfully applied to inclusive CCQE neutrino scattering and, most recently, to the full inelastic regime for both electron and neutrino reactions. The description of the 2p2h channel has also been included in the model on the basis of the fully relativistic calculation of refs. [45,46]. The corresponding model for the quasielastic region (SuSAv2-QE) is based on a set of QE scaling functions extracted from the relativistic mean field (RMF) model for the nucleus.

Although it has been shown that the SuSAv2 model gives an accurate description of inclusive electron and neutrino cross section measurements, this model is mostly suited at intermediate and high values of the momentum transfer where scaling works. Additionally, the SuSAv2 model cannot be directly applied to more exclusive measurements like $(e, e'p)$ [47] or semi-inclusive neutrino-nucleus cross sections [48–50] where a lepton is detected in coincidence with another particle, usually an ejected nucleon. To overcome these issues the energy-dependent relativistic mean field (ED-RMF) model, based on the relativistic distorted-wave impulse approximation (RDWIA) [47,51–53], has been proposed [54,55]. In this model, the wave function used to describe the initial nuclear state that interacts with the neutrino corresponds to the eigenstates solution of the Dirac equation using the RMF potentials. To include effects beyond the mean-field approximation an additional s-shell is parameterized to reproduce the high missing energy profile given by the Benhar spectral function model [51–53]. In contrast with the typical cascade FSI model used by generators, in this model the same RMF potentials used for the description of the initial state are used to solve the Dirac equation and find the scattering states that describe the ejected nucleon wave function. By adopting this approach the preservation of orthogonality, also known as Pauli blocking, is guaranteed and the distortion of the outgoing nucleon is considered by propagating it using the self-energy calculated within the mean-field approach. However using a pure RMF approach with an energy-independent potential to describe the nucleon in the final state is bound to be inadequate as the momentum of the final nucleon increases. This is because the RMF potentials are too strong for relatively high nucleon momenta, when one would expect the potentials to become weaker. This issue is solved by employing a linear combination of the SuSAv2 scaling functions derived from the relativistic plane-wave impulse approximation and the RMF model, with the weight of each contribution determined by a transition function that varies with the momentum transfer q . The parameters of the model were fitted to $^{12}\text{C}(e, e')$ data, resulting in remarkable agreement with inclusive data, particularly for ω values exceeding approximately 50 MeV [26,56]. This agreement extends to (e, e') data from different nuclei as well as to inclusive CC neutrino-nucleus reactions. The radial dependencies of both ED-RMF and RMF potentials for ^{12}C are compared in Figure 1 for different values of the proton kinetic energy T_N . For small values of T_N both potentials are essentially the same, preserving orthogonality between initial and final states that is especially relevant in this low-momentum region. At larger

values of T_N , orthogonality is no longer an issue and the transition function reduces the magnitude of the strong RMF potentials improving the agreement with inclusive electron and neutrino scattering data.

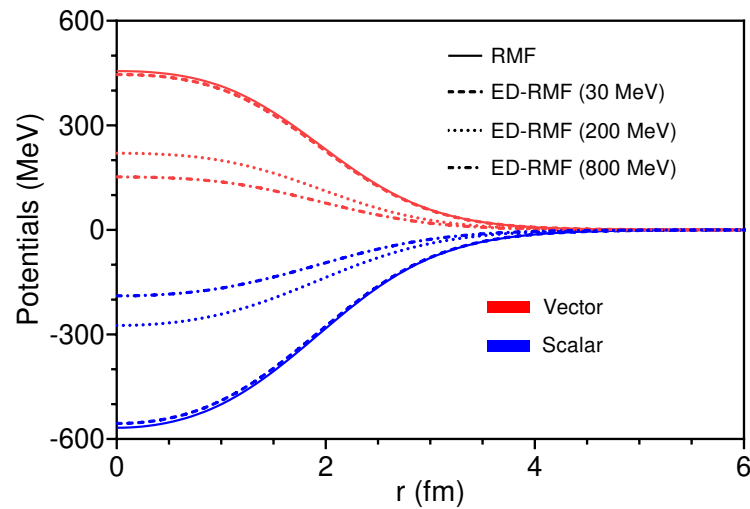


Figure 1. Energy-dependent relativistic mean field (ED-RMF) potential [26,54] for ^{12}C evaluated at different proton kinetic energies $T_N = 30$ MeV (dashed), 200 MeV (dotted) and 800 MeV (dash-dotted). The RMF potential (solid) is also shown for reference. The vector (red lines) and scalar (blue lines) components of the potentials are shown separately.

We compare the 1p1h cross section with two alternative model predictions from the NEUT event generator [57]. Like other neutrino event generators, NEUT uses a factorization approach in order to generate neutrino-nucleus interactions. This means that events are sampled according to an interaction cross-section corresponding to a product of the single nucleon cross-section (following the Llewellyn-Smith formalism [58]) and a nuclear ground state probability distribution. Final state interactions (FSI) are further factorized, described by placing outgoing hadrons through an intranuclear cascade [59].

We select two models from NEUT. The first one is the Local Fermi Gas (LFG) model, based on the prescription from [60] and implemented as described in [61]. In this scheme, the nucleon removal energy and momentum distribution depends on the local nuclear density. In addition, nuclear effects such as long-range correlations are incorporated via a Random Phase Approximation (RPA) approach, which causes a suppression of the cross-section at low values of the four-momentum transfer. The NEUT LFG model is similar to the one implemented in GENIE [62,63], which is used as an input to analyses from the NOvA and MicroBooNE experiments.

The second is a spectral function (SF) model following the prescription from Benhar et al. [64]. This approach provides a more realistic description of the nuclear ground state which takes into account the shell structure of the nucleus as well as the presence of short-range correlations (SRC). The SF model relies on the plane-wave impulse-approximation (PWIA) to write the cross section as a product of the single nucleon component and a two-dimensional probability distribution as a function of the individual nucleon removal energy and momentum. The position, strength and width of the individual shells (manifested as peaks in the removal energy distribution) have been extracted from exclusive electron scattering measurements, with additional theory-based contributions for correlated nucleon pairs, mostly in the high momentum and removal energy region. This is the model used by the T2K experiment in its neutrino oscillation analyses [65].

2.2. 2p2h-MEC Channel

The description of the 2p2h channel that will be used in this work is based on the fully relativistic calculation of ref. [46]. This is a RFG-based model of two-particle two-hole

excitations induced by weak meson-exchange currents (MEC) for inclusive CC neutrino scattering. The model extends a previous calculation performed for electron scattering [45] which encompasses all the many-body diagrams involving the exchange of a pion and the emission of two nucleons, including also the possible excitation of an intermediate Δ resonance, which plays a dominant role. Notably, the calculation exactly accounts for the anti-symmetry of the nuclear wave function.

The model has been also implemented in the GENIE event generator [66,67] to speed up demanding calculations and to ease comparison with electron and neutrino data. The implementation of the 2p2h model in this generator is based on an inclusive microscopic calculation, where a sum is performed over all the hadronic variables, although GENIE is able to predict a detailed final state under some assumptions. Only recently the model has been extended to the semi-inclusive channel for electron scattering [68] and it will be further generalised to neutrino reactions. It should be stressed, however, that for the inclusive results shown in the present work the agreement between the results of the microscopic calculation and those provided by GENIE is excellent [66]. Further improvements of the model are also under way in order to go beyond the RFG description of the ground state [69] and achieve a better consistency between the nuclear models used to describe the different reaction channels.

2.3. Inelastic Contributions

In a recent work [70], the superscaling model SuSAv2, initially developed for CCQE neutrino-nucleus cross sections, was extended to the full inelastic regime (SuSAv2-inelastic), where the resonance production and deep inelastic contributions were described via the extension to the neutrino sector of the SuSAv2 inelastic model originally developed for (e, e') reactions. The model has been widely and successfully tested against electron-carbon, argon and oxygen data.

The model merges inelastic structure functions [71–79] to describe the nucleon behavior in the inelastic regime with the superscaling/RMF approach to describe the nuclear dynamics. The structure functions come from QCD analyses, parton distribution functions (PDFs) or phenomenological approaches (Bodek-Ritchie or Bosted-Christy) and are combined with RMF-based scaling functions used in the SuSAv2-QE approach but adapted to the inelastic domain in order to describe the nuclear dynamics [70]. In this sense, the different inelastic contributions are considered by means of the final-state invariant mass that acts as an inelasticity parameter. Thus, the inelastic regime can be splitted into different contributions by integrating over different ranges of the invariant mass in the inelastic nuclear responses. More details about this formalism can be found in [70].

Given that the inelastic structure functions are based on (e, e') reactions, some approximations must be made to define the W_3 weak structure functions. In the case of PDFs, these contributions can be derived from the antiquark distribution via the parton model. For the structure functions provided by Bodek-Ritchie or Bosted-Christy, W_3 can be built through the use of phenomenological expressions [21,70,75].

In this study, we employ a recent update of the SuSAv2-inelastic approach, which incorporates the inelastic inclusive structure function derived from the Dynamical-Coupled Channels model (DCC) [36,38]. Specifically, the DCC inelastic structure functions consider the resonance region up to an invariant mass of 2.1 GeV and a squared four-momentum of 3.0 GeV². For contributions beyond this range, we adopt the Bodek-Ritchie inelastic structure functions to characterize the deep inelastic scattering region. The features of this model can be found in [80]. Extensive validation has been conducted against T2K, MicroBooNE, MINERvA, and ArgoNEUT inclusive neutrino scattering datasets. While some underestimation is observed at MINERvA kinematics, in general our model produces accurate comparisons with data. In Section 3, we delve into a comparative analysis of the differences presented by the SuSAv2-inelastic model for neutrino and antineutrino scattering.

Additionally, we also consider the effects of pion-absorption within the nucleus by means of the NEUT simulation. The NEUT single pion production simulation is based

on the Rein-Sehgal model for single pion production. Pion absorption effects occurs when a pion created in a primary neutrino-nucleus interaction is absorbed within the nuclear medium as simulated by NEUT's FSI cascade, which can cause the nucleus to emit additional protons or neutrons. Within this inelastic interaction, the energy lost can create an important uncertainty in determining the energy of the incident neutrino. Thus, pion absorption processes are particularly important because a pion production event can have a QE-like topology in the final state.

3. Discussion of Results

In what follows, the results obtained in this work are analyzed in two subsections related, respectively, to the study of T2K neutrino and antineutrino $CC0\pi$ data, and CC inclusive cross sections at T2K and MINERvA kinematics where all inelasticities are considered.

3.1. Comparison with T2K $CC0\pi$ Data

In Figures 2–6 we show the comparison of the different inclusive theoretical models described in the previous section with the T2K combined measurement of inclusive $CC0\pi$ muon neutrino— (ν_μ, μ^-) —and antineutrino— $(\bar{\nu}_\mu, \mu^+)$ —cross sections [9], as well as their sum, difference and asymmetry. Double differential cross sections with respect to the outgoing lepton momentum p_μ and scattering angle θ are represented versus p_μ in different bins of $\cos\theta$. The neutrino-antineutrino asymmetry is defined as

$$\mathcal{A} = \frac{d\sigma_\nu - d\sigma_{\bar{\nu}}}{d\sigma_\nu + d\sigma_{\bar{\nu}}}, \quad (1)$$

which results in an observable that stresses not only the neutrino-antineutrino contrasts but also focuses on the vector-axial transverse interference term (T'_{VA}) and their associated form factors. In the particular case of using the same neutrino and antineutrino fluxes (or fixed energies), the neutrino-antineutrino difference roughly represents the VA interference term which would be mostly canceled if we consider the neutrino-antineutrino sum. In Tables 1–5 we also show the $\chi^2/d.o.f.$ value for each angular bin. One can see that none of the models is able to describe the measured neutrino and antineutrino cross sections for all the kinematics. For both neutrinos and antineutrinos measurements, we can appreciate small differences between the predictions of the theoretical models for backward muon angles. However, as we move to more forward muon scattering angles, the SuSAv2 and SF models overestimate the experimental data more than the ED-RMF and LFG models. Specifically the differences between SuSAv2 and ED-RMF predictions can be attributed to the better description of low-energy nuclear effects by the latter compared to the former. Also, although the SF model is a quite realistic model, an incomplete implementation of the model in NEUT or the addition of a 2p2h simulation modeled using RFG as nuclear model could explain why this model fails at forward lepton scattering angles.

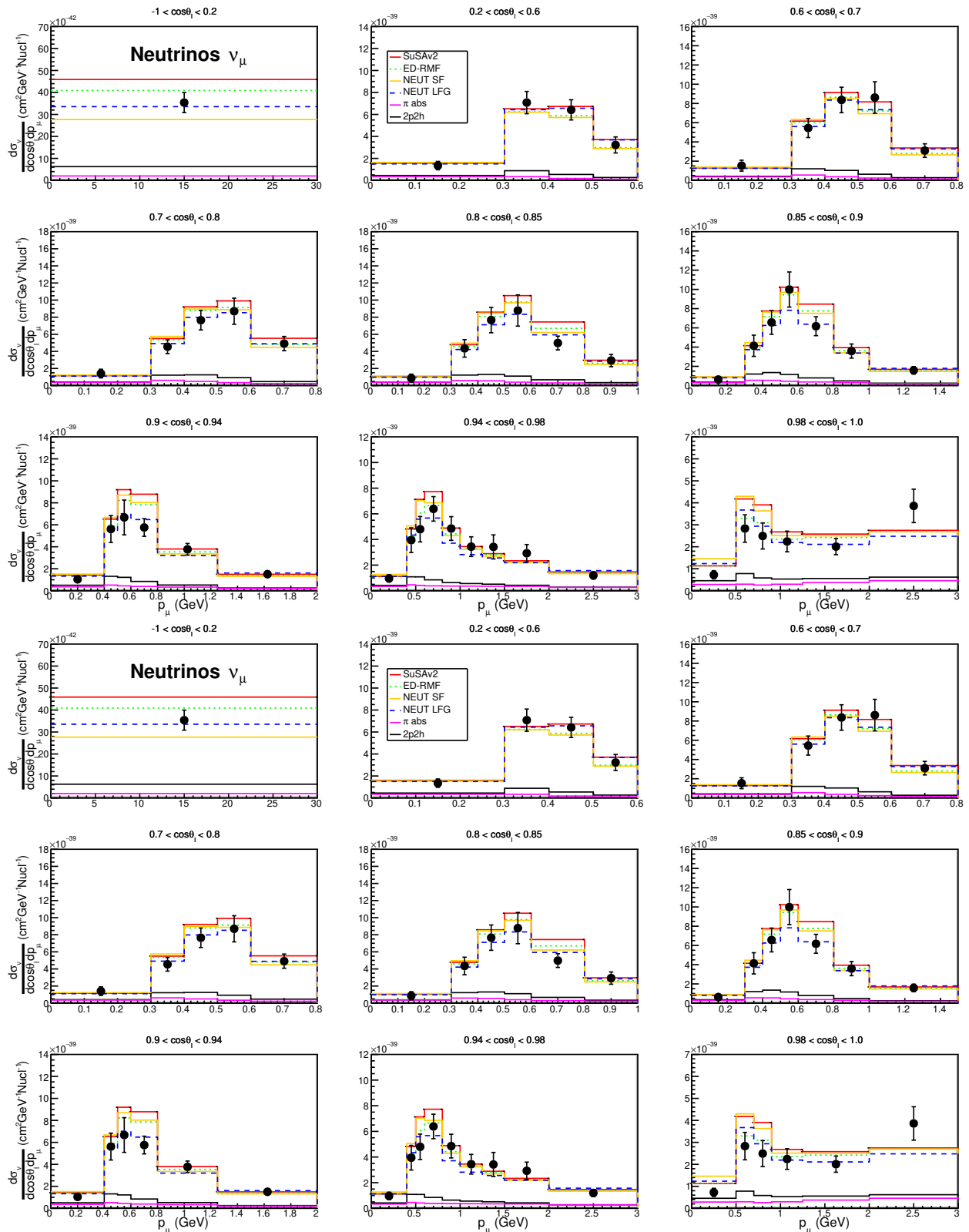


Figure 2. T2K ν_μ CC0 π double-differential cross-section per nucleon in bins of true muon kinematics. The results are compared to NEUT LFG, NEUT SF, ED-RMF and SuSAv2 models. The contribution of 2p2h and π absorption are also shown separately, which are common and are already included in all previous models. The measurement is taken from [9].

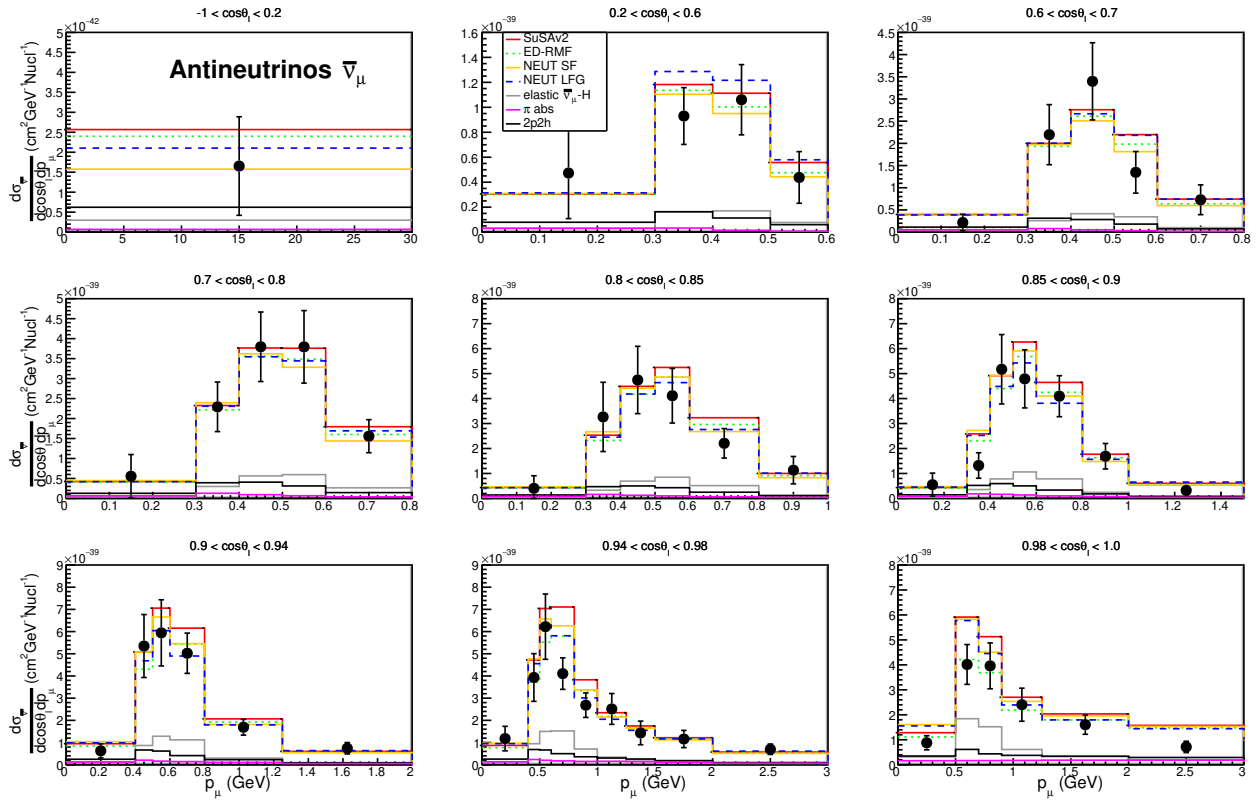


Figure 3. Same as Figure 2 but for antineutrinos. The curve corresponding to the elastic $\bar{\nu}_\mu$ -H contribution is shown separately and is included in all models. The measurement is taken from [9].

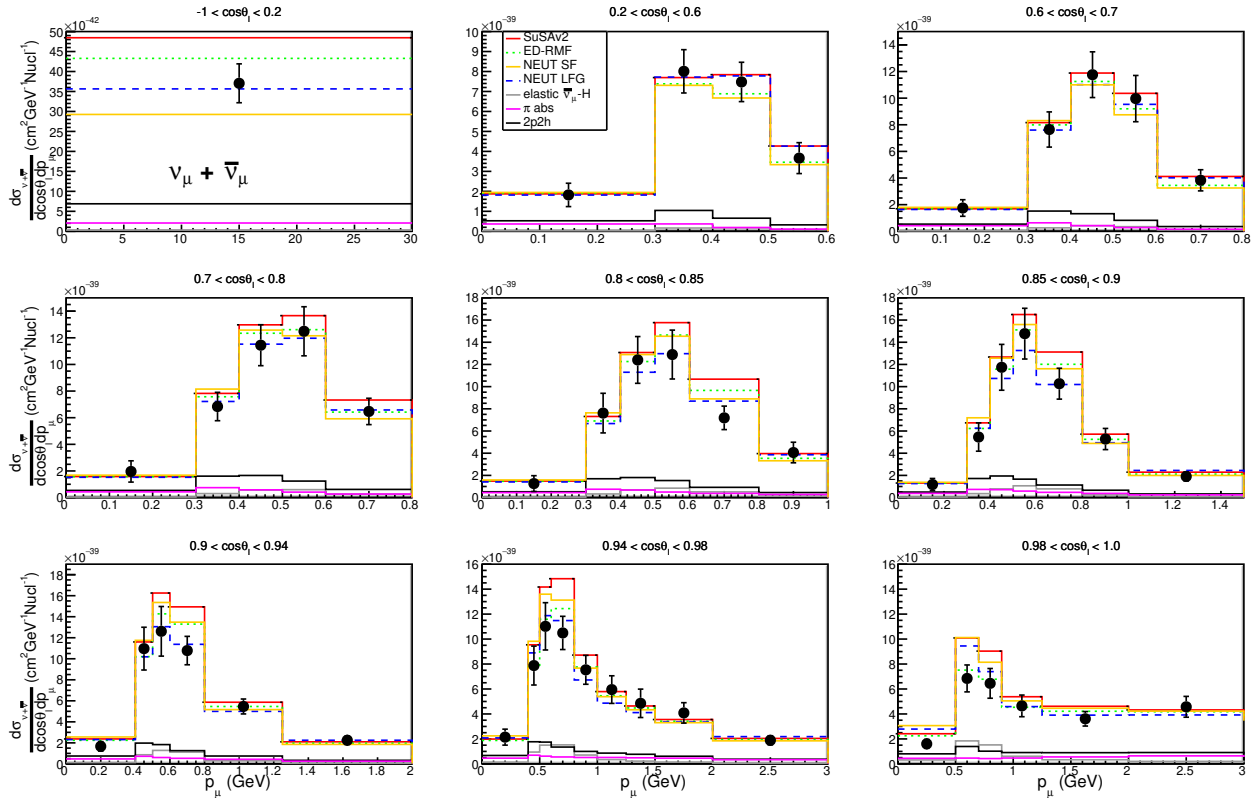


Figure 4. Same as Figure 2 but for the double-differential $\nu_\mu + \bar{\nu}_\mu$ CC0 π cross-section sum. The measurement is taken from [9].

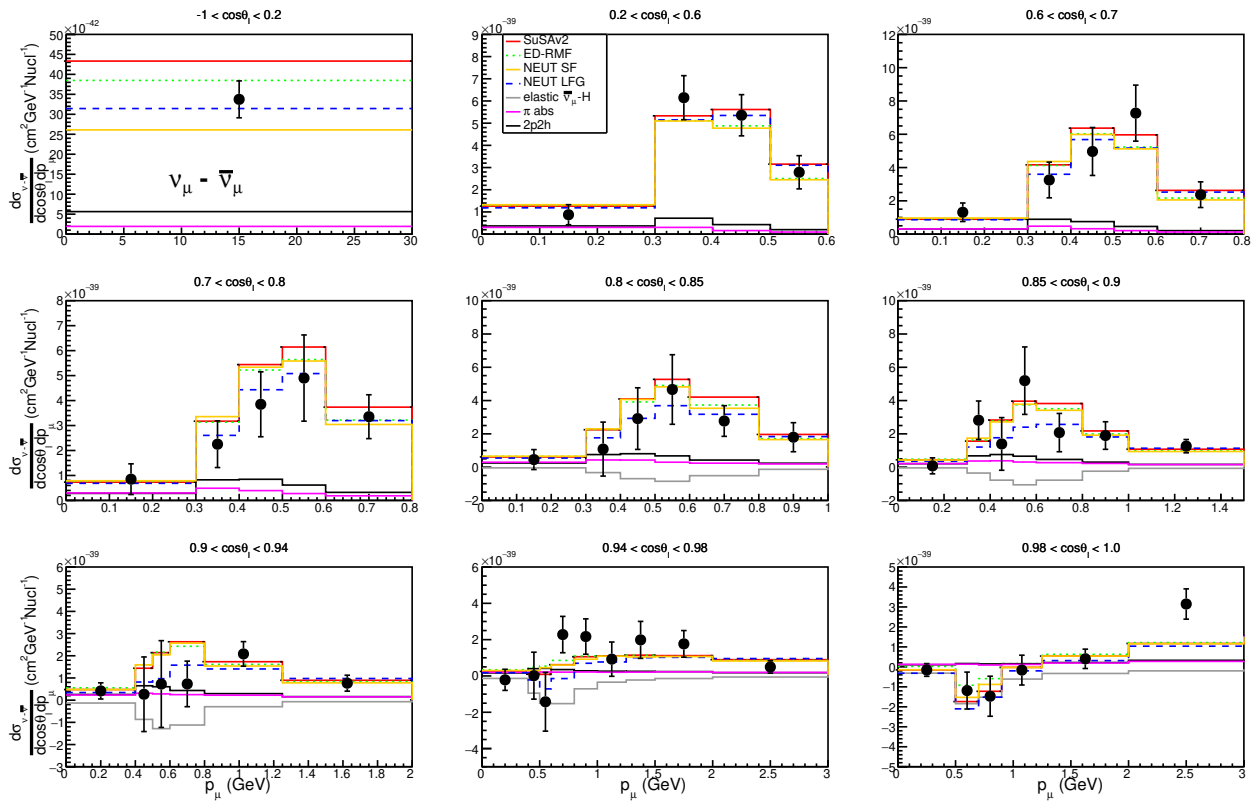


Figure 5. Same as Figure 2 but for the double-differential $\nu_\mu - \bar{\nu}_\mu$ CC0 π cross-section difference. The measurement is taken from [9].

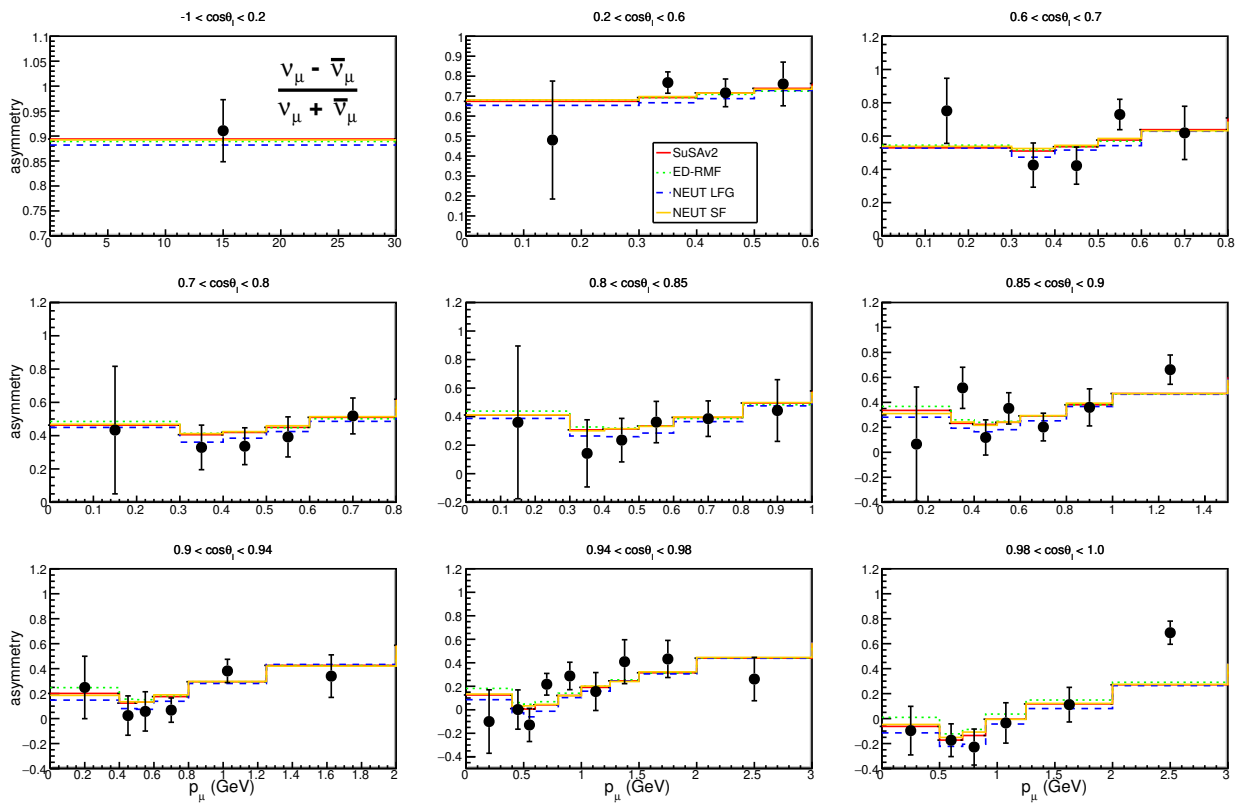


Figure 6. Same as Figure 2 but for the double-differential cross-section asymmetry. The measurement is taken from [9].

Table 1. $\chi^2/d.o.f.$ values for T2K CC0 π results on neutrinos. The second row of each $\cos\theta_\mu$ bin corresponds to excluding the most right and left experimental data points from the $\chi^2/d.o.f.$ calculation. Number of data points considered in each particular bin are shown in parentheses.

$\cos(\theta_\mu)$ (<i>d.o.f.</i>)	ED-RMF	SuSAv2	LFG	SF
$-1 < \cos(\theta_\mu) < 0.2$ (1)	2.44	8.92	0.28	4.83
$0.2 < \cos(\theta_\mu) < 0.6$ (5)	0.56	1.86	2.11	0.72
$0.2 < \cos(\theta_\mu) < 0.6$ (3)	0.61	0.70	0.64	0.83
$0.6 < \cos(\theta_\mu) < 0.7$ (6)	0.84	0.39	0.30	1.37
$0.6 < \cos(\theta_\mu) < 0.7$ (4)	0.92	0.49	0.33	1.58
$0.7 < \cos(\theta_\mu) < 0.8$ (6)	1.01	1.46	0.32	1.92
$0.7 < \cos(\theta_\mu) < 0.8$ (4)	1.07	1.83	0.17	2.26
$0.8 < \cos(\theta_\mu) < 0.85$ (7)	1.56	3.14	0.59	1.12
$0.8 < \cos(\theta_\mu) < 0.85$ (5)	2.11	4.39	0.65	1.35
$0.85 < \cos(\theta_\mu) < 0.9$ (8)	1.02	1.96	1.46	0.88
$0.85 < \cos(\theta_\mu) < 0.9$ (6)	0.96	1.98	0.74	0.85
$0.90 < \cos(\theta_\mu) < 0.94$ (7)	3.61	6.21	1.35	5.66
$0.90 < \cos(\theta_\mu) < 0.94$ (5)	4.55	8.25	1.12	6.78
$0.94 < \cos(\theta_\mu) < 0.98$ (10)	1.18	2.79	1.93	3.06
$0.94 < \cos(\theta_\mu) < 0.98$ (8)	1.37	3.42	2.18	3.38
$0.98 < \cos(\theta_\mu) < 1.0$ (8)	6.77	10.16	3.91	8.29
$0.98 < \cos(\theta_\mu) < 1.0$ (6)	1.71	5.28	2.30	5.05

Table 2. $\chi^2/d.o.f.$ values for T2K CC0 π results on antineutrinos. The second row of each $\cos\theta_\mu$ bin corresponds to excluding the most right and left experimental data points from the $\chi^2/d.o.f.$ calculation. Number of data points considered in each particular bin are shown in parentheses.

$\cos(\theta_\mu)$ (<i>d.o.f.</i>)	ED-RMF	SuSAv2	LFG	SF
$-1 < \cos(\theta_\mu) < 0.2$ (1)	0.71	1.07	0.26	0.01
$0.2 < \cos(\theta_\mu) < 0.6$ (5)	0.61	0.71	1.36	0.67
$0.2 < \cos(\theta_\mu) < 0.6$ (3)	0.54	1.00	2.15	0.48
$0.6 < \cos(\theta_\mu) < 0.7$ (6)	1.06	1.47	1.40	1.05
$0.6 < \cos(\theta_\mu) < 0.7$ (4)	1.03	1.61	1.58	0.78
$0.7 < \cos(\theta_\mu) < 0.8$ (6)	0.30	0.22	0.18	0.55
$0.7 < \cos(\theta_\mu) < 0.8$ (4)	0.12	0.17	0.19	0.34
$0.8 < \cos(\theta_\mu) < 0.85$ (7)	1.10	1.66	0.54	0.73
$0.8 < \cos(\theta_\mu) < 0.85$ (5)	1.24	2.09	0.71	0.67
$0.85 < \cos(\theta_\mu) < 0.9$ (8)	1.77	2.74	3.12	2.28
$0.85 < \cos(\theta_\mu) < 0.9$ (6)	2.35	3.64	4.11	2.98
$0.90 < \cos(\theta_\mu) < 0.94$ (7)	0.83	1.46	0.61	1.19
$0.90 < \cos(\theta_\mu) < 0.94$ (5)	0.69	1.40	0.18	0.51
$0.94 < \cos(\theta_\mu) < 0.98$ (10)	1.90	4.72	1.56	2.78
$0.94 < \cos(\theta_\mu) < 0.98$ (8)	2.20	5.67	1.90	3.25
$0.98 < \cos(\theta_\mu) < 1.0$ (8)	5.98	7.79	5.60	6.69
$0.98 < \cos(\theta_\mu) < 1.0$ (6)	5.34	6.28	4.72	5.68

Table 3. $\chi^2/d.o.f.$ values for T2K CC0 π results on the neutrino and antineutrino sum. The second row of each $\cos\theta_\mu$ bin corresponds to excluding the most right and left experimental data points from the $\chi^2/d.o.f.$ calculation. Number of data points considered in each particular bin are shown in parentheses.

$\cos(\theta_\mu)$ (d.o.f.)	ED-RMF	SuSAv2	LFG	SF
$-1 < \cos(\theta_\mu) < 0.2$ (1)	2.78	9.31	0.14	4.35
$0.2 < \cos(\theta_\mu) < 0.6$ (5)	0.28	0.62	0.69	0.51
$0.2 < \cos(\theta_\mu) < 0.6$ (3)	0.40	0.63	0.58	0.67
$0.6 < \cos(\theta_\mu) < 0.7$ (6)	0.44	0.11	0.12	0.92
$0.6 < \cos(\theta_\mu) < 0.7$ (4)	0.33	0.14	0.17	0.84
$0.7 < \cos(\theta_\mu) < 0.8$ (6)	0.77	0.91	0.22	1.79
$0.7 < \cos(\theta_\mu) < 0.8$ (4)	0.41	0.99	0.13	1.58
$0.8 < \cos(\theta_\mu) < 0.85$ (7)	2.31	3.92	0.92	1.50
$0.8 < \cos(\theta_\mu) < 0.85$ (5)	2.93	5.38	1.19	1.63
$0.85 < \cos(\theta_\mu) < 0.9$ (8)	0.51	1.28	1.05	0.72
$0.85 < \cos(\theta_\mu) < 0.9$ (6)	0.65	1.69	1.16	0.90
$0.90 < \cos(\theta_\mu) < 0.94$ (7)	2.38	4.55	0.94	4.40
$0.90 < \cos(\theta_\mu) < 0.94$ (5)	2.57	5.62	0.45	4.13
$0.94 < \cos(\theta_\mu) < 0.98$ (10)	1.35	4.69	1.57	3.39
$0.94 < \cos(\theta_\mu) < 0.98$ (8)	1.49	5.57	1.96	3.98
$0.98 < \cos(\theta_\mu) < 1.0$ (8)	5.94	11.68	5.89	9.18
$0.98 < \cos(\theta_\mu) < 1.0$ (6)	0.51	5.09	2.95	4.56

Table 4. $\chi^2/d.o.f.$ values for T2K CC0 π results on the neutrino and antineutrino difference. The second row of each $\cos\theta_\mu$ bin corresponds to excluding the most right and left experimental data points from the $\chi^2/d.o.f.$ calculation. Number of data points considered in each particular bin are shown in parentheses.

$\cos(\theta_\mu)$ (d.o.f.)	ED-RMF	SuSAv2	LFG	SF
$-1 < \cos(\theta_\mu) < 0.2$ (1)	1.80	7.35	0.42	4.68
$0.2 < \cos(\theta_\mu) < 0.6$ (5)	1.02	1.85	1.94	1.12
$0.2 < \cos(\theta_\mu) < 0.6$ (3)	0.89	0.78	0.83	1.02
$0.6 < \cos(\theta_\mu) < 0.7$ (6)	1.20	0.90	0.83	1.49
$0.6 < \cos(\theta_\mu) < 0.7$ (4)	1.59	1.10	0.94	2.04
$0.7 < \cos(\theta_\mu) < 0.8$ (6)	0.87	1.51	0.34	1.14
$0.7 < \cos(\theta_\mu) < 0.8$ (4)	1.29	2.00	0.22	1.70
$0.8 < \cos(\theta_\mu) < 0.85$ (7)	0.64	1.28	0.31	0.55
$0.8 < \cos(\theta_\mu) < 0.85$ (5)	0.82	1.60	0.21	0.69
$0.85 < \cos(\theta_\mu) < 0.9$ (8)	1.24	1.57	1.50	1.11
$0.85 < \cos(\theta_\mu) < 0.9$ (6)	1.04	1.26	1.11	0.97
$0.90 < \cos(\theta_\mu) < 0.94$ (7)	1.70	1.85	1.07	1.81
$0.90 < \cos(\theta_\mu) < 0.94$ (5)	2.04	2.13	0.89	2.28
$0.94 < \cos(\theta_\mu) < 0.98$ (10)	1.43	1.37	2.22	1.56
$0.94 < \cos(\theta_\mu) < 0.98$ (8)	1.67	1.64	2.69	1.87
$0.98 < \cos(\theta_\mu) < 1.0$ (8)	2.39	2.12	2.16	1.74
$0.98 < \cos(\theta_\mu) < 1.0$ (6)	2.36	2.16	2.68	2.30

Table 5. $\chi^2/d.o.f.$ values for T2K CC0 π results on the asymmetry. The second row of each $\cos\theta_\mu$ bin corresponds to excluding the most right and left experimental data points from the $\chi^2/d.o.f.$ calculation. Number of data points considered in each particular bin are shown in parentheses.

$\cos(\theta_\mu)$ (<i>d.o.f.</i>)	ED-RMF	SuSAv2	LFG	SF
$-1 < \cos(\theta_\mu) < 0.2$ (1)	0.24	0.14	0.42	0.17
$0.2 < \cos(\theta_\mu) < 0.6$ (5)	1.19	1.23	1.92	1.11
$0.2 < \cos(\theta_\mu) < 0.6$ (3)	1.43	1.33	2.67	1.18
$0.6 < \cos(\theta_\mu) < 0.7$ (6)	1.61	1.57	1.90	1.51
$0.6 < \cos(\theta_\mu) < 0.7$ (4)	1.85	1.67	2.13	1.66
$0.7 < \cos(\theta_\mu) < 0.8$ (6)	0.68	0.70	0.29	0.80
$0.7 < \cos(\theta_\mu) < 0.8$ (4)	0.78	0.73	0.22	0.88
$0.8 < \cos(\theta_\mu) < 0.85$ (7)	0.36	0.34	0.25	0.34
$0.8 < \cos(\theta_\mu) < 0.85$ (5)	0.36	0.31	0.26	0.31
$0.85 < \cos(\theta_\mu) < 0.9$ (8)	1.51	1.58	1.85	1.51
$0.85 < \cos(\theta_\mu) < 0.9$ (6)	1.67	1.74	2.15	1.69
$0.90 < \cos(\theta_\mu) < 0.94$ (7)	1.27	1.10	0.80	1.21
$0.90 < \cos(\theta_\mu) < 0.94$ (5)	1.46	1.17	0.71	1.33
$0.94 < \cos(\theta_\mu) < 0.98$ (10)	1.67	1.70	2.13	1.78
$0.94 < \cos(\theta_\mu) < 0.98$ (8)	1.92	2.02	2.59	2.12
$0.98 < \cos(\theta_\mu) < 1.0$ (8)	6.84	6.98	6.54	6.74
$0.98 < \cos(\theta_\mu) < 1.0$ (6)	7.68	7.94	7.72	8.04

Since the difference between the neutrino and antineutrino cross sections, shown in Figure 5, is driven by the vector-axial (VA) response, which has opposite sign in the two cases, the sum of the two cross sections, shown in Figure 4, is approximately twice the sum of the vector-vector (VV) and axial-axial (AA) cross sections. We observe that different nuclear models can yield very different contributions for both the sum and the difference, but these effects roughly cancel in the asymmetry, shown in Figure 6. This is in contrast with the simulations shown in Figures 23 and 24 of ref. [9] where the spread between the nuclear models shown is largely canceled for both the cross section difference and the asymmetry. This can be explained by the different models used to estimate the 2p2h contributions which are the SuSAv2 model in this work and the Valencia model in [9]. In Figure 5 we can see that the cross section difference is negative for some of the bins, which is caused by the additional elastic $\bar{\nu}_\mu$ -H contribution present in the antineutrino measurement which can lead to higher cross sections than for neutrinos at some particular kinematics.

3.2. Analysis of CC Inclusive Results at T2K and MINERvA Kinematics

In this section we compare the neutrino and the antineutrino CC inclusive cross section given by the SuSAv2 model using the inclusive DCC approach for the resonance regime and the inclusive Bodek-Ritchie parametrization of the inelastic structure functions. We consider all possible channels, namely QE, 2p2h, RES, SIS and DIS. We use the SuSAv2 inclusive model for our analysis, which lacks additional degrees of freedom and is not fine-tuned. This model maintains consistency while preventing double counting in the inelastic region: this is achieved by carefully bounding the integral limits over the invariant mass W_X of the hadronic final states. In our analysis, we compare various data sets under identical kinematic conditions, i.e., including the same flux and studying the same kinematical bins, to better compare the influence of the vector-axial (VA) interference term. This represents the main difference between neutrino and antineutrino cross sections, being positive for neutrinos and negative for antineutrinos. We perform this analysis at different energies, using the T2K and MINERvA fluxes, which are shown in Figure 7. It is worth noticing that these fluxes exhibit distinct features: while the T2K flux peaks around $E_\nu \sim 0.8$ GeV [9],

the MINERvA flux peaks at a significantly higher energy of $E_\nu \sim 6$ GeV, with a more pronounced tail [81].

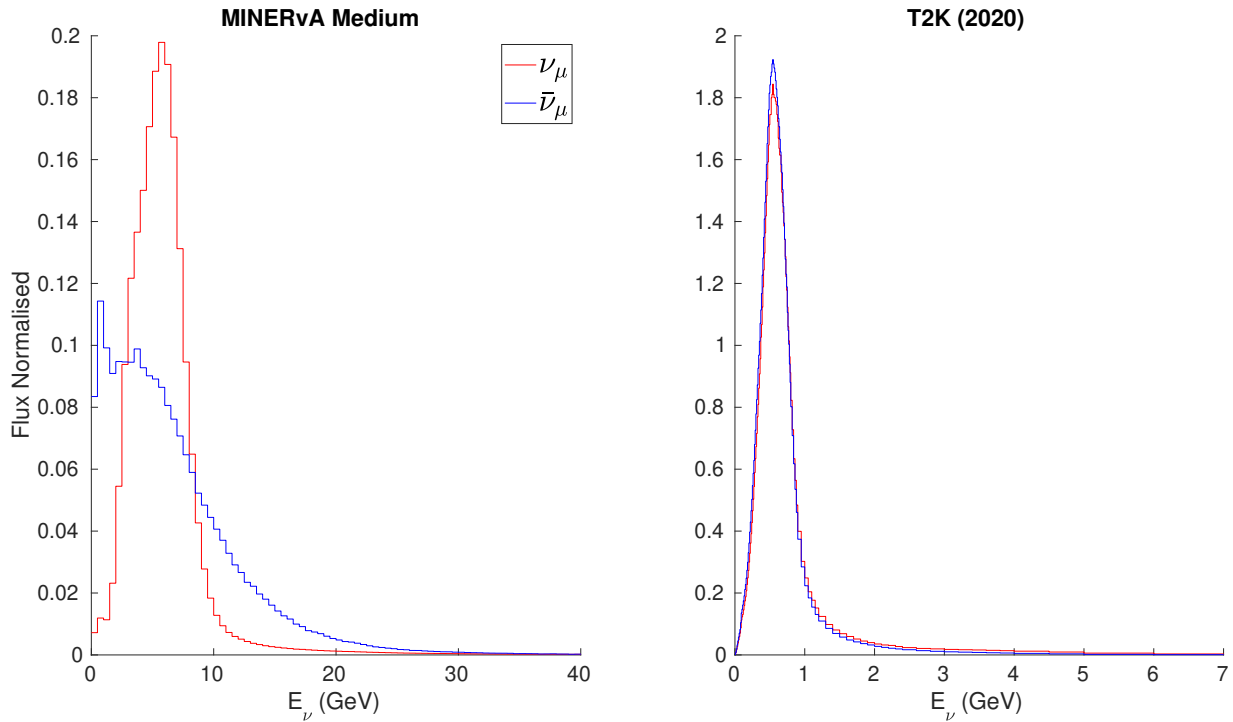


Figure 7. Normalised antineutrino and neutrino FHC fluxes from MINERvA (**left**) peaking at $E_\nu \sim 6$ GeV and RHC antineutrino and FHC neutrino fluxes for T2K (**right**) peaking at $E_\nu \sim 0.8$ GeV .

In Figure 8, we present a comparison of the double-differential inclusive cross sections for neutrinos (solid line) and antineutrinos (dashed line), utilizing only the $\bar{\nu}_\mu$ fluxes from T2K (red lines) and MINERvA (blue lines) in both neutrino and antineutrino calculations. This provides a more direct comparison of neutrino vs. antineutrino differences when considering the same flux in both cases, respectively, stressing the differences associated to the VA interference response. Particularly at very backward angles, a substantial gap is observed between the ν_μ and $\bar{\nu}_\mu$ cross sections, which gradually diminishes as the scattering angle decreases, notably evident at very forward angles. Moreover, at these forward angles, the MINERvA cross section surpasses that of T2K, while the opposite trend is observed at very forward angles.

In Figures 9 and 10, we compare neutrino and antineutrino cross sections against T2K and MINERvA data. In particular, we present the discrepancies between the ν_μ and $\bar{\nu}_\mu$ inclusive double-differential cross sections employing both ν_μ and $\bar{\nu}_\mu$ fluxes for both neutrino and antineutrino calculations in order to stress the neutrino-antineutrino differences in similar conditions.

For T2K, we observe a near resemblance between neutrino cross sections for both ν_μ and $\bar{\nu}_\mu$ fluxes at very backward angles. The same is true for the antineutrino cross sections, yet the total result is strongly reduced due to negative contribution of the VA term. However, important differences can be observed using both fluxes for the neutrino cross sections and also for the antineutrino ones at forward angles and large p_μ , which are due to the more pronounced high-energy tail of the ν_μ flux with respect to the $\bar{\nu}_\mu$ one.

When comparing neutrino and antineutrino cross sections using the same fluxes, we observe that the differences are very important at backward angles, as commented above, which implies a remarkable relevance of the VA component. On the contrary, the VA term is less dominant as long as we move to forward angles where the neutrino and antineutrino cross sections are more similar, apart from the region of large p_μ .

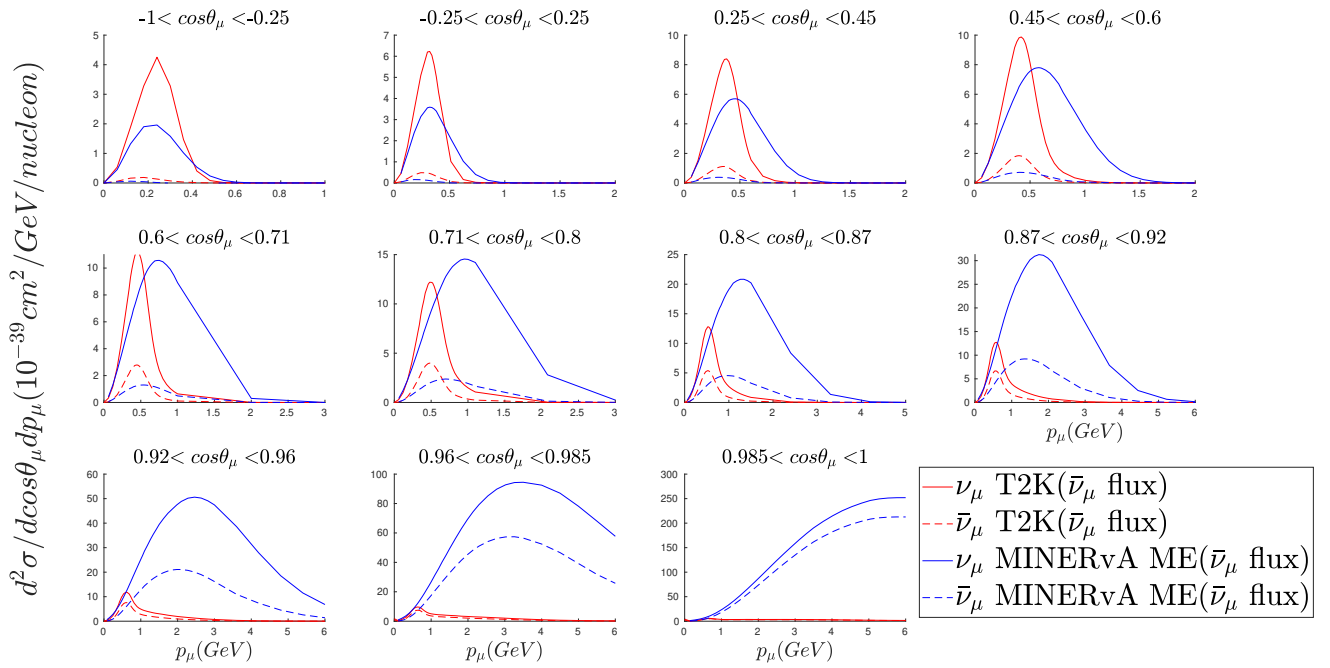


Figure 8. Comparison of neutrino and antineutrino CC-inclusive cross sections at T2K and MINERvA kinematics. As indicated in the panel, the T2K antineutrino flux has been used to produce both neutrino and antineutrino results. The same applies to the MINERvA case.

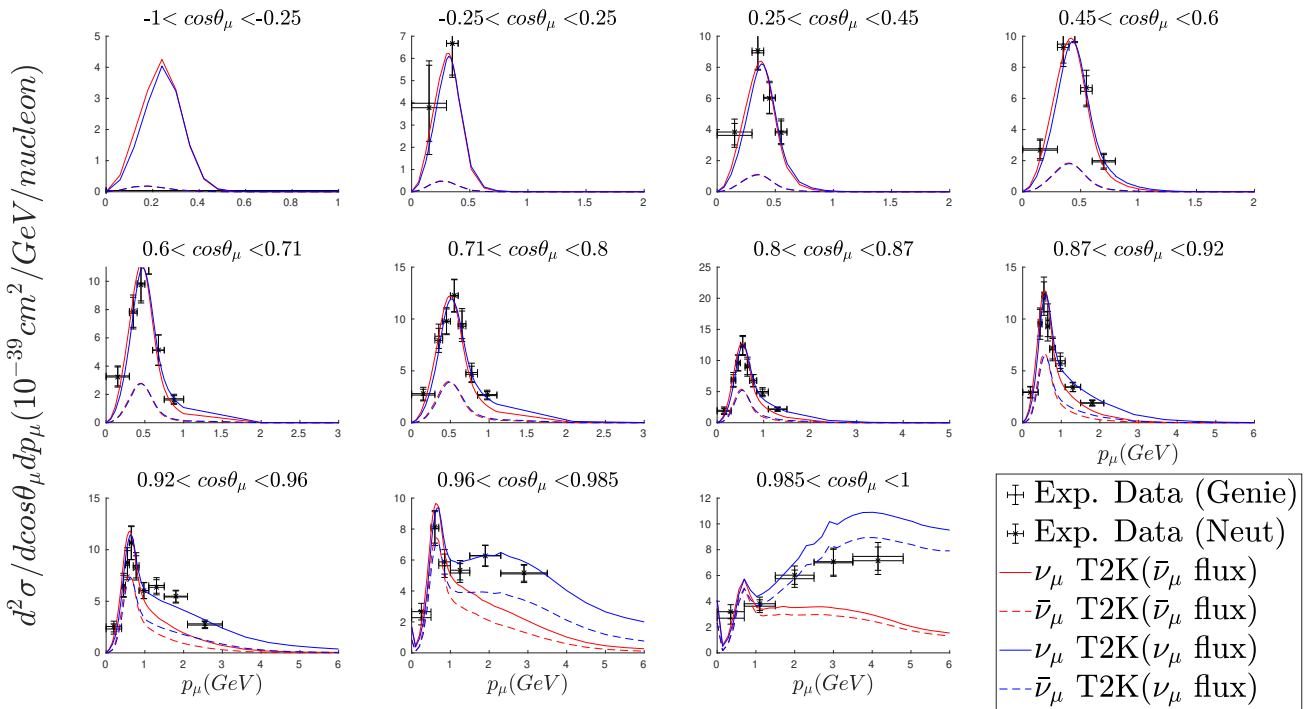


Figure 9. Comparison of neutrino and antineutrino CC-inclusive cross sections at T2K kinematics. As indicated in the panel, the T2K neutrino and antineutrino fluxes have been used, separately, to produce both neutrino and antineutrino results. Comparisons have been performed with T2K neutrino CC inclusive data [13].

Regarding the comparison with the T2K CC-inclusive neutrino data, our neutrino model using the neutrino flux yields an overall good agreement with these measurements. Nevertheless, there is a noticeable overestimation at low muon momentum values and very forward angles, mostly due to our QE contribution. At these specific kinematics,

related to low- q , the SUSAv2-QE model tends to overestimate the data due to the treatment of low-energy nuclear effects. This could be corrected by using a relativistic mean-field (RMF) or an energy-dependent mean field (ED-RMF) model where the description of nuclear-medium effects at low kinematics is more accurate. This issue will be addressed in further work.

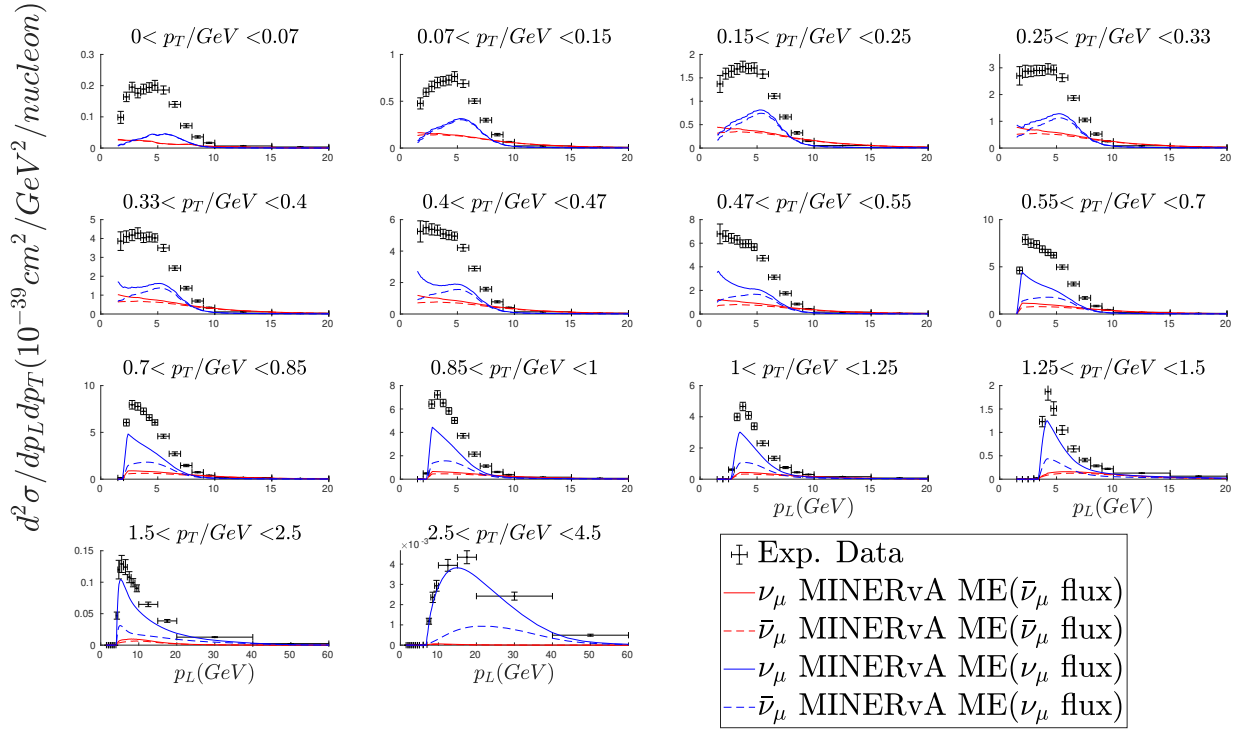


Figure 10. Comparison of neutrino and antineutrino CC-inclusive cross sections at MINERvA kinematics. As indicated in the panel, the MINERvA neutrino and antineutrino fluxes have been used, separately, to produce both neutrino and antineutrino results. Comparisons have been performed with MINERvA neutrino CC inclusive data [81].

In the case of MINERvA, the neutrino and antineutrino cross sections derived from the $\bar{\nu}_\mu$ flux are in general smaller than those from the ν_μ flux. When using the same fluxes, the discrepancy between ν_μ and $\bar{\nu}_\mu$ cross sections increases with the transverse momentum value ($p_T = p_\mu \sin\theta_\mu$), i.e., it is more relevant at backward angles, while the opposite behavior is observed for the longitudinal momentum ($p_L = p_\mu \cos\theta$): this is again connected with the magnitude of the VA term, the main difference between neutrino and antineutrino cross sections when the same flux is considered. With regard to MINERvA neutrino CC inclusive data, our model tends to underestimate these measurements, as also shown in [80]. Specifically, our resonance model produces results much lower than the ones from the models used in generators [81]. This discrepancy might arise from the lack of non-resonant processes in our model or from the data reconstruction methods that employ a resonance model where nuclear effects are somehow less relevant, thus assuming more events in the resonance channel. A more detailed analysis of these findings can be found in [80]. Due to the lack of MINERvA antineutrino inclusive measurements we cannot make a more complete comparison for this particular case.

4. Conclusions

In this work we present a study of the neutrino and antineutrino differences via the analysis of neutrino-nucleus cross sections at T2K and MINERvA kinematics. The ED-RMF and SuSAv2 neutrino interaction models have proved to successfully describe the sum, difference and asymmetry of $CC0\pi$ neutrino and antineutrino cross sections. On the contrary, they underestimate significantly the data at MINERvA kinematics, mainly at backward

angles, which could be ascribed to the differences between the resonance model employed in this work and the tuned model used in generators, that are more prominent at high kinematics. Furthermore, unlike the T2K analysis, effects coming from pion absorptions were not considered when comparing with MINERvA data, which are expected to be included in future works. Further studies are also required with regard to the description of the resonant and inelastic structure functions within the SuSAv2-inelastic framework.

Additionally, a χ^2 analysis was carried out to quantify the goodness of the agreement and compare with the one reported in the experimental papers and the NEUT and GENIE simulations. We have found that, in general, the SuSAv2 model produces larger values of χ^2 than those obtained by the simulations and the ED-RMF model. These discrepancies need further investigation. However, it should be stressed that our models do not contain any free parameter or additional tuning to compare with data. In future works, we plan to implement other resonance models such as the MK approach in the SuSAv2 framework and other nucleon form factors for the QE regime. Also, the recent inclusion of the DCC model in the NEUT simulator will allow for a direct comparison with our resonant predictions.

Overall, the present study, with the use of different neutrino interaction models, will allow to shed light on the nuclear effects involved in the (anti)neutrino-nucleus interactions. A precise understanding of the limitations and uncertainties of these approaches and their implementation in generators will be essential for the next generation of neutrino oscillation experiments. In particular, the difference between neutrino and antineutrino cross sections studied in this manuscript is a promising observable to explore sensitivity to different nuclear models and weak nucleon form factors. These analyses need to be extended with more statistics and improved systematics uncertainties together with more exclusive measurements that also provide detailed information about hadron kinematics in the final state. This will help to reduce nuclear-medium uncertainties in neutrino experiments and to improve model selection for oscillation analyses and the determination of CPV in the neutrino sector.

Author Contributions: Conceptualization, S.J.D., G.D.M., L.M., M.B.B. and J.A.C.; methodology, J.M.F.-P., A.N.G.-O., J.G.-R., S.J.D., G.D.M. and L.M.; software, J.M.F.-P., A.N.G.-O., J.G.-R., S.J.D., G.D.M. and L.M.; validation and formal analysis, J.M.F.-P., A.N.G.-O., J.G.-R., S.J.D., G.D.M. and L.M.; writing, review and editing, J.M.F.-P., J.G.-R., S.J.D., G.D.M., L.M., J.A.C. and M.B.B. All authors have read and agreed to the published version of the manuscript.

Funding: This work has been partially supported by the Spanish Ministerio de Ciencia e Innovación and ERDF (European Regional Development Fund) under Contract No. PID2020-114687GB-100, by the Junta de Andalucía (FQM 160, SOMM17/6105/UGR and P20-01247); it is supported in part by the University of Tokyo ICRR's Inter-University Research Program FY2022 (Ref. 2022i-J-001) & FY2023 (Ref. 2023i-J-001). J.G.-R. was supported by a Contract PIF VI-PPITUS 2020 from the University of Seville (Plan Propio de Investigación y Transferencia) associated with the project PID2020-114687GB-100. MBB acknowledges support from INFN under the National Project NUCSYS.

Data Availability Statement: Data are contained within the article.

Conflicts of Interest: The authors declare no conflict of interest. The funders had no role in the design of the study; in the collection, analyses, or interpretation of data; in the writing of the manuscript; or in the decision to publish the results.

Abbreviations

The following abbreviations are used in this manuscript:

CP	Charge-Parity
CPV	Charge-Parity Violation
QE	Quasielastic
CC	Charged-Current
CCQE	Charged-Current Quasielastic
RES	Resonance

DCC	Dynamical Coupled-Channels
DIS	Deep Inelastic Scattering
SIS	Shallow Inelastic Scattering
2p2h	two-particle - two-hole
PDF	Parton Distribution Function
QCD	Quantum Chromodynamics
FSI	Final State Interactions
SuSA	SuperScaling Approach
SuSAv2	SuperScaling Approach version 2
RMF	Relativistic Mean Field
ED-RMF	Energy Dependent - Relativistic Mean Field
PWIA	Plane Wave Impulse Approximation
RDWIA	Relativistic Distorted Wave Impulse Approximation
SRC	Short-Range Correlations
RFG	Relativistic Fermi Gas
LFG	Local Fermi Gas
SF	Spectral Function
d.o.f.	degrees of freedom

References

- Esteban, I.; Gonzalez-Garcia, M.C.; Maltoni, M.; Schwetz, T.; Zhou, A. The fate of hints: Updated global analysis of three-flavor neutrino oscillations. *J. High Energy Phys.* **2020**, *9*, 178. [[CrossRef](#)]
- Workman, R.L.; Burkert, V.D.; Crede, V.; Klempt, E.; Thoma, U.; Tiator, L.; Agashe, K.; Aielli, G.; Allanach, B.C.; Amsler, C.; et al. Review of Particle Physics. *Prog. Theor. Exp. Phys.* **2022**, *2022*, 083C01. [[CrossRef](#)]
- Maki, Z.; Nakagawa, M.; Sakata, S. Remarks on the Unified Model of Elementary Particles. *Prog. Theor. Phys.* **1962**, *28*, 870–880. [[CrossRef](#)]
- Bilenky, S.M.; Pontecorvo, B. Lepton Mixing and Neutrino Oscillations. *Phys. Rept.* **1978**, *41*, 225–261. [[CrossRef](#)]
- T2K Collaboration. Constraint on the matter–antimatter symmetry-violating phase in neutrino oscillations. *Nature* **2020**, *580*, 339–344; Erratum in *Nature* **2020**, *583*, E16. [[CrossRef](#)]
- Hyper-Kamiokande Proto-Collaboration. Hyper-Kamiokande Design Report. *arXiv* **2018**, arXiv:1805.04163.
- DUNE Collaboration. Long-Baseline Neutrino Facility (LBNF) and Deep Underground Neutrino Experiment (DUNE) Conceptual Design Report Volume 2: The Physics Program for DUNE at LBNF. *arXiv* **2016**, arXiv:1512.06148.
- Alvarez-Ruso, L.; Athar, M.S.; Barbaro, M.B.; Cherdack, D.; Christy, M.E.; Coloma, P.; Donnelly, T.W.; Dytman, S.; de Gouvêa, A.; Hill, R.J.; et al. NuSTEC White Paper: Status and challenges of neutrino–nucleus scattering. *Prog. Part. Nucl. Phys.* **2018**, *100*, 1–68. [[CrossRef](#)]
- Abe, K.; Akhlaq, N.; Akutsu, R.; Ali, A.; Alt, C.; Andreopoulos, C.; Anthony, L.; Antonova, M.; Aoki, S.; Ariga, A.; et al. First combined measurement of the muon neutrino and antineutrino charged-current cross section without pions in the final state at T2K. *Phys. Rev. D* **2020**, *101*, 112001. [[CrossRef](#)]
- Abratenko, P.; Adams, C.; Alrashed, M.; An R.; Anthony, J.; Asaadi, J.; Ashkenazi, A.; Auger, M.; Balasubramanian, S.; Baller, B.; et al. First Measurement of Inclusive Muon Neutrino Charged Current Differential Cross Sections on Argon at $E_\nu \sim 0.8$ GeV with the MicroBooNE Detector. *Phys. Rev. Lett.* **2019**, *123*, 131801. [[CrossRef](#)]
- Acerro, M.A.; Adamson, P.; Aliaga, L.; Anfimov, N.; Antoshkin, A.; Arrieta-Diaz, E.; Asquith, L.; Aurisano, A.; Back, A.; Baird, M.; et al. Measurement of the ν_e -Nucleus Charged-Current Double-Differential Cross Section at $\langle E_\nu \rangle = 2.4$ GeV using NOvA. *Phys. Rev. Lett.* **2023**, *130*, 051802. [[CrossRef](#)] [[PubMed](#)]
- Filkins, A.; Ruterbories, D.; Liu, Y.; Dar, Z.A.; Akbar, F.; Altinok, O.; Andrade, D.A.; Ascencio, M.V.; Bashyal, A.; Bercellie, A.; et al. Double-differential inclusive charged-current ν_μ cross sections on hydrocarbon in MINERvA at $\langle E_\nu \rangle \sim 3.5$ GeV. *Phys. Rev. D* **2020**, *101*, 112007. [[CrossRef](#)]
- Abe, K.; Amey, J.; Andreopoulos, C.; Anthony, L.; Antonova, M.; Aoki, S.; Ariga, A.; Ashida, Y.; Azuma, Y.; Ban, S.; et al. Measurement of inclusive double-differential ν_μ charged-current cross section with improved acceptance in the T2K off-axis near detector. *Phys. Rev. D* **2018**, *98*, 012004. [[CrossRef](#)]
- Abe, K.; Akhlaq, N.; Akutsu, R.; Ali, A.; Alt, C.; Andreopoulos, C.; Anthony, L.; Antonova, M.; Aoki, S.; Ariga, A.; et al. Measurement of the charged-current electron (anti-)neutrino inclusive cross-sections at the T2K off-axis near detector ND280. *J. High Energy Phys.* **2020**, *2020*, 114. [[CrossRef](#)]
- Acciarri, R.; Adams, C.; Asaadi, J.; Baller, B.; Bolton, T.; Bromberg, C.; Cavanna, F.; Church, E.; Edmunds, D.; Ereditato, A.; et al. Measurements of inclusive muon neutrino and antineutrino charged current differential cross sections on argon in the NuMI antineutrino beam. *Phys. Rev. D* **2014**, *89*, 112003. [[CrossRef](#)]
- MiniBooNE Collaboration. First measurement of the muon neutrino charged current quasielastic double differential cross section. *Phys. Rev. D* **2010**, *81*, 092005. [[CrossRef](#)]

17. ArgoNeuT Collaboration. First Measurements of Inclusive Muon Neutrino Charged Current Differential Cross Sections on Argon. *Phys. Rev. Lett.* **2012**, *108*, 161802. [[CrossRef](#)] [[PubMed](#)]
18. Barbaro, M.B.; Caballero, J.A.; Donnelly, T.W.; Maieron, C. Inelastic electron-nucleus scattering and scaling at high inelasticity. *Phys. Rev. C* **2004**, *69*, 035502. [[CrossRef](#)]
19. Sato, T.; Lee, T.S.H. Dynamical models of the excitations of nucleon resonances. *J. Phys. G Nucl. Part. Phys.* **2009**, *36*, 073001. [[CrossRef](#)]
20. CLAS Collaboration. Measurement of the polarized structure function $\sigma_{LT'}$ for $p(\vec{e}, e'p)\pi^0$ in the $\Delta(1232)$ resonance region. *Phys. Rev. C* **2003**, *68*, 032201. [[CrossRef](#)]
21. Athar, M.S.; Morfín, J.G. Neutrino(antineutrino)–nucleus interactions in the shallow- and deep-inelastic scattering regions. *J. Phys. G Nucl. Part. Phys.* **2021**, *48*, 034001. [[CrossRef](#)]
22. Martini, M.; Ericson, M.; Chanfray, G.; Marteau, J. Unified approach for nucleon knock-out and coherent and incoherent pion production in neutrino interactions with nuclei. *Phys. Rev. C* **2009**, *80*, 065501. [[CrossRef](#)]
23. González-Jiménez, R.; Niewczas, K.; Jachowicz, N. Pion production within the hybrid relativistic plane wave impulse approximation model at MiniBooNE and MINERvA kinematics. *Phys. Rev. D* **2018**, *97*, 013004. [[CrossRef](#)]
24. Barbaro, M.B.; De Pace, A.; Fiume, L. The SuSA Model for Neutrino Oscillation Experiments: From Quasielastic Scattering to the Resonance Region. *Universe* **2021**, *7*, 140. [[CrossRef](#)]
25. Vagnoni, E.; Benhar, O.; Meloni, D. Inelastic Neutrino-Nucleus Interactions within the Spectral Function Formalism. *Phys. Rev. Lett.* **2017**, *118*, 142502. [[CrossRef](#)] [[PubMed](#)]
26. González-Jiménez, R.; Nikolakopoulos, A.; Jachowicz, N.; Udías, J.M. Nuclear effects in electron-nucleus and neutrino-nucleus scattering within a relativistic quantum mechanical framework. *Phys. Rev. C* **2019**, *100*, 045501. [[CrossRef](#)]
27. Singh, S.K.; Vicente-Vacas, M.J.; Oset, E. Nuclear effects in neutrino production of δ at intermediate energies. *Phys. Lett. B* **1998**, *416*, 23–28. [[CrossRef](#)]
28. Praet, C.; Lalakulich, O.; Jachowicz, N.; Ryckebusch, J. Δ -mediated pion production in nuclei. *Phys. Rev. C* **2009**, *79*, 044603. [[CrossRef](#)]
29. Ivanov, M.V.; Megias, G.D.; González-Jiménez, R.; Moreno, O.; Barbaro, M.B.; Caballero, J.A.; Donnelly, T.W. Charged-current inclusive neutrino cross sections in the superscaling model including quasielastic, pion production and meson-exchange contributions. *J. Phys. G Nucl. Part. Phys.* **2016**, *43*, 045101. [[CrossRef](#)]
30. Rein, D.; Sehgal, L.M. Neutrino-excitation of baryon resonances and single pion production. *Ann. Phys.* **1981**, *133*, 79–153. [[CrossRef](#)]
31. Fogli, G.; Nardulli, G. A new approach to the charged current induced weak one-pion production. *Nucl. Phys. B* **1979**, *160*, 116–150. [[CrossRef](#)]
32. Lalakulich, O.; Paschos, E.A.; Piranishvili, G. Resonance production by neutrinos: The second resonance region. *Phys. Rev. D* **2006**, *74*, 014009. [[CrossRef](#)]
33. Schreiner, P.A.; von Hippel, F. $\nu p \rightarrow \mu^{--} \Delta^{++}$: Comparison with Theory. *Phys. Rev. Lett.* **1973**, *30*, 339–342. [[CrossRef](#)]
34. Kabirnezhad, M. Single pion production in neutrino-nucleon interactions. *Phys. Rev. D* **2018**, *97*, 013002. [[CrossRef](#)]
35. Kabirnezhad, M. Single-pion production in electron-proton interactions. *Phys. Rev. C* **2023**, *107*, 025502. [[CrossRef](#)]
36. Nakamura, S.; Kamano, H.; Sato, T. Dynamical coupled-channels model for neutrino-induced meson productions in resonance region. *Phys. Rev. D* **2015**, *92*, 074024. [[CrossRef](#)]
37. Nakamura, S.X.; Kamano, H.; Sato, T. Impact of final state interactions on neutrino-nucleon pion production cross sections extracted from neutrino-deuteron reaction data. *Phys. Rev. D* **2019**, *99*, 031301. [[CrossRef](#)]
38. Osaka University. Website of the ANL-Osaka DCC Model. 2021. Available online: <https://www.rcnp.osaka-u.ac.jp/~anl-osk/> (accessed on 15 October 2023)
39. Donnelly, T.W.; Sick, I. Superscaling in inclusive electron-nucleus scattering. *Phys. Rev. Lett.* **1999**, *82*, 3212–3215. [[CrossRef](#)]
40. Amaro, J.E.; Barbaro, M.B.; Caballero, J.A.; González-Jiménez, R.; Megias, G.D.; Simo, I.R. Electron- versus neutrino-nucleus scattering. *J. Phys. G Nucl. Part. Phys.* **2020**, *47*, 124001. [[CrossRef](#)]
41. Amaro, J.E.; Barbaro, M.B.; Caballero, J.A.; Donnelly, T.W.; González-Jiménez, R.; Megias, G.D.; Ruiz Simo, I. Neutrino-nucleus scattering in the SuSA model. *Eur. Phys. J. Spec. Top.* **2021**, *230*, 4321–4338. [[CrossRef](#)]
42. Megias, G.; Amaro, J.; Barbaro, M.; Caballero, J.; Donnelly, T. Inclusive electron scattering within the SuSAv2 meson-exchange current approach. *Phys. Rev. D* **2016**, *94*, 013012. [[CrossRef](#)]
43. Megias, G.; Amaro, J.; Barbaro, M.; Caballero, J.; Donnelly, T.; Simo, I.R. Charged-current neutrino-nucleus reactions within the superscaling meson-exchange current approach. *Phys. Rev. D* **2016**, *94*, 093004. [[CrossRef](#)]
44. Megias, G.D.; Barbaro, M.B.; Caballero, J.A.; Amaro, J.E.; Donnelly, T.W.; Simo, I.R.; Orden, J.W.V. Neutrino–oxygen CC0 Π scattering in the SuSAv2-MEC model. *J. Phys. G Nucl. Part. Phys.* **2018**, *46*, 015104. [[CrossRef](#)]
45. De Pace, A.; Nardi, M.; Alberico, W.M.; Donnelly, T.W.; Molinari, A. The 2p-2h electromagnetic response in the quasielastic peak and beyond. *Nucl. Phys. A* **2003**, *726*, 303–326. [[CrossRef](#)]
46. Simo, I.R.; Amaro, J.E.; Barbaro, M.B.; Pace, A.D.; Caballero, J.A.; Donnelly, T.W. Relativistic model of 2p-2h meson exchange currents in (anti)neutrino scattering. *J. Phys. G Nucl. Part. Phys.* **2017**, *44*, 065105. [[CrossRef](#)]
47. Udías, J.M.; Sarriguren, P.; Moya de Guerra, E.; Garrido, E.; Caballero, J.A. Spectroscopic factors in ^{40}Ca and ^{208}Pb from $(e, e'p)$: Fully relativistic analysis. *Phys. Rev. C* **1993**, *48*, 2731–2739. [[CrossRef](#)] [[PubMed](#)]

48. Moreno, O.; Donnelly, T.W.; Van Orden, J.W.; Ford, W.P. Semi-inclusive charged-current neutrino-nucleus reactions. *Phys. Rev. D* **2014**, *90*, 013014. [[CrossRef](#)]
49. Van Orden, J.W.; Donnelly, T.W. Nuclear theory and event generators for charge-changing neutrino reactions. *Phys. Rev. C* **2019**, *100*, 044620. [[CrossRef](#)]
50. Franco-Patino, J.M.; Gonzalez-Rosa, J.; Caballero, J.A.; Barbaro, M.B. Semi-inclusive charged-current neutrino-nucleus cross sections in the relativistic plane-wave impulse approximation. *Phys. Rev. C* **2020**, *102*, 064626. [[CrossRef](#)]
51. González-Jiménez, R.; Barbaro, M.B.; Caballero, J.A.; Donnelly, T.W.; Jachowicz, N.; Megias, G.D.; Niewczas, K.; Nikolakopoulos, A.; Van Orden, J.W.; Udías, J.M. Neutrino energy reconstruction from semi-inclusive samples. *Phys. Rev. C* **2022**, *105*, 025502. [[CrossRef](#)]
52. Franco-Patino, J.M.; González-Jiménez, R.; Dolan, S.; Barbaro, M.B.; Caballero, J.A.; Megias, G.D.; Udías, J.M. Final state interactions in semi-inclusive neutrino-nucleus scattering: Applications to the T2K and MINERvA experiments. *Phys. Rev. D* **2022**, *106*, 113005. [[CrossRef](#)]
53. Franco-Patino, J.M.; Dolan, S.; González-Jiménez, R.; Barbaro, M.B.; Caballero, J.A.; Megias, G.D. New model comparison for semi-inclusive charged-current electron and muon neutrino scattering by ^{40}Ar in the energy range of the MicroBooNE experiment. *Phys. Rev. D* **2024**, *109*, 013004. [[CrossRef](#)]
54. Gonzalez-Jimenez, R.; Barbaro, M.B.; Caballero, J.A.; Donnelly, T.W.; Jachowicz, N.; Megias, G.D.; Niewczas, K.; Nikolakopoulos, A.; Udías, J.M. Constraints in modeling the quasielastic response in inclusive lepton-nucleus scattering. *Phys. Rev. C* **2020**, *101*, 015503. [[CrossRef](#)]
55. Gonzalez-Jimenez, R.; Megias, G.D.; Barbaro, M.B.; Caballero, J.A.; Donnelly, T.W. Extensions of superscaling from relativistic mean field theory: The SuSAv2 model. *Phys. Rev. C* **2014**, *90*, 035501. [[CrossRef](#)]
56. Lu, X.G.; Pickering, L.; Dolan, S.; Barr, G.; Coplowe, D.; Uchida, Y.; Wark, D.; Wascko, M.O.; Weber, A.; Yuan, T. Measurement of nuclear effects in neutrino interactions with minimal dependence on neutrino energy. *Phys. Rev. C* **2016**, *94*, 015503. [[CrossRef](#)]
57. Hayato, Y.; Pickering, L. The NEUT neutrino interaction simulation program library. *Eur. Phys. J. Spec. Top.* **2021**, *230*, 4469–4481. [[CrossRef](#)]
58. Llewellyn Smith, C.H. Neutrino Reactions at Accelerator Energies. *Phys. Rept.* **1972**, *3*, 261–379. [[CrossRef](#)]
59. Dytman, S.; Hayato, Y.; Raboanary, R.; Sobczyk, J.T.; Tena-Vidal, J.; Vololoniaina, N. Comparison of validation methods of simulations for final state interactions in hadron production experiments. *Phys. Rev. D* **2021**, *104*, 053006. [[CrossRef](#)]
60. Gran, R.; Nieves, J.; Sanchez, F.; Vicente Vacas, M.J. Neutrino-nucleus quasi-elastic and 2p2h interactions up to 10 GeV. *Phys. Rev. D* **2013**, *88*, 113007. [[CrossRef](#)]
61. Bourguille, B.; Nieves, J.; Sánchez, F. Inclusive and exclusive neutrino-nucleus cross sections and the reconstruction of the interaction kinematics. *JHEP* **2021**, *4*, 4. [[CrossRef](#)]
62. Andreopoulos, C.; Bell, A.; Bhattacharya, D.; Cavanna, F.; Dobson, J.; Dytman, S.; Gallagher, H.; Guzowski, P.; Hatcher, R.; Kehayias, P.; et al. The GENIE Neutrino Monte Carlo Generator. *Nucl. Instrum. Meth.* **2010**, *A614*, 87–104. [[CrossRef](#)]
63. Andreopoulos, C.; Barry, C.; Dytman, S.; Gallagher, H.; Golan, T.; Hatcher, R.; Perdue, G.; Yarba, J. The GENIE Neutrino Monte Carlo Generator: Physics and User Manual. *arXiv* **2015**, arXiv:1510.05494.
64. Benhar, O.; Fabrocini, A.; Fantoni, S.; Sick, I. Spectral function of finite nuclei and scattering of GeV electrons. *Nucl. Phys. A* **1994**, *579*, 493–517. [[CrossRef](#)]
65. Abe, K.; Akhlaq, N.; Akutsu, R.; Ali, A.; Alonso Monsalve, S.; Alt, C.; Andreopoulos, C.; Antonova, M.; Aoki, S.; Arihara, T.; et al. Measurements of neutrino oscillation parameters from the T2K experiment using 3.6×10^{21} protons on target. *Eur. Phys. J. C* **2023**, *83*, 782. [[CrossRef](#)] [[PubMed](#)]
66. Dolan, S.; Megias, G.D.; Bolognesi, S. Implementation of the SuSAv2-meson exchange current 1p1h and 2p2h models in GENIE and analysis of nuclear effects in T2K measurements. *Phys. Rev. D* **2020**, *101*, 033003. [[CrossRef](#)]
67. Papadopoulou, A.; Ashkenazi, A.; Gardiner, S.; Betancourt, M.; Dytman, S.; Weinstein, L.B.; Piasetzky, E.; Hauenstein, F.; Khachatryan, M.; Dolan, S.; et al. Inclusive electron scattering and the genie neutrino event generator. *Phys. Rev. D* **2021**, *103*, 113003. [[CrossRef](#)]
68. Belocchi, V.; Barbaro, M.B.; De Pace, A.; Martini, M. Relativistic meson-exchange currents in semi-inclusive lepton scattering *arXiv* **2024**, arXiv:2401.13640.
69. Casale, P.R.; Amaro, J.E.; Barbaro, M.B. Meson-Exchange Currents in Quasielastic Electron Scattering in a Generalized Superscaling Approach. *Symmetry* **2023**, *15*, 1709. [[CrossRef](#)]
70. Gonzalez-Rosa, J.; Megias, G.; Caballero, J.; Barbaro, M. SuSAv2 model for inelastic neutrino-nucleus scattering. *Phys. Rev. D* **2022**, *105*, 093009. [[CrossRef](#)]
71. Collaboration, T.N.; Ball, R.D.; Bertone, V.; Cerutti, F.; Del Debbio, L.; Forte, S.; Guffanti, A.; Latorre, J.I.; Rojo, J.; Ubiali, M. Unbiased global determination of parton distributions and their uncertainties at NNLO and at LO. *arXiv* **2011**, arXiv:1107.2652.
72. Bjorken, J.D. Asymptotic Sum Rules at Infinite Momentum. *Phys. Rev.* **1969**, *179*, 1547–1553. [[CrossRef](#)]
73. Tooran, A.G.; Khorramian, A.; Abdolmaleki, H. QCD analysis of structure functions in deep inelastic neutrino-nucleon scattering without using the orthogonal polynomials approach. *Phys. Rev. C* **2019**, *99*, 035207. [[CrossRef](#)]
74. Bodek, A.; Breidenbach, M.; Dubin, D.L.; Elias, J.E.; Friedman, J.I.; Kendall, H.W.; Poucher, J.S.; Riordan, E.M.; Sogard, M.R.; Coward, D.H.; et al. Experimental studies of the neutron and proton electromagnetic structure functions. *Phys. Rev. D* **1979**, *20*, 1471–1552. [[CrossRef](#)]

75. Bodek, A.; Ritchie, J.L. Fermi-motion effects in deep-inelastic lepton scattering from nuclear targets. *Phys. Rev. D* **1981**, *23*, 1070–1091. [[CrossRef](#)]
76. Callan, C.G.; Gross, D.J. High-Energy Electroproduction and the Constitution of the Electric Current. *Phys. Rev. Lett.* **1969**, *22*, 156–159. [[CrossRef](#)]
77. CCFR Collaboration. An Improved Determination of α_s from Neutrino-Nucleon Scattering. *Phys. Rev. Lett.* **1997**, *79*, 1213. [[CrossRef](#)]
78. Kim, J.H.; Harris, D.A.; Arroyo, C.G.; De Barbaro, L.; De Barbaro, P.; Bazarko, A.O.; Bernstein, R.H.; Bodek, A.; Bolton, T.; Budd, H.; et al. A Measurement of s from the Gross-Llewellyn Smith Sum Rule. *Phys. Rev. Lett.* **1998**, *81*, 3595. [[CrossRef](#)]
79. Gehrmann, T.; Roberts, R.G.; Whalley, M.R. A compilation of structure functions in deep inelastic scattering *J. Phys. G* **1999**, *25*, A1. [[CrossRef](#)]
80. Gonzalez-Rosa, J.; Megias, G.D.; Caballero, J.A.; Barbaro, M.B.; Franco-Patino, J.M. Superscaling in the resonance region for neutrino-nucleus scattering: The SuSAv2 dynamical coupled-channels model. *Phys. Rev. D* **2023**, *108*, 113008. [[CrossRef](#)]
81. Ruterbories, D.; Filkins, A.; Ahmad Dar, Z.; Akbar, F.; Andrade, D.A.; Ascencio, M.V.; Bashyal, A.; Bellantoni, L.; Bercellie, A.; Betancourt, M.; et al. Measurement of inclusive charged-current ν_μ cross sections as a function of muon kinematics at $\langle E_\nu \rangle \sim 6$ GeV on hydrocarbon. *Phys. Rev. D* **2021**, *104*, 092007. [[CrossRef](#)]

Disclaimer/Publisher's Note: The statements, opinions and data contained in all publications are solely those of the individual author(s) and contributor(s) and not of MDPI and/or the editor(s). MDPI and/or the editor(s) disclaim responsibility for any injury to people or property resulting from any ideas, methods, instructions or products referred to in the content.